Chinese Journal of Chemical Engineering 60 (2023) 108–117

Contents lists available at ScienceDirect

Chinese Journal of Chemical Engineering

journal homepage: www.elsevier.com/locate/CJChE

Full Length Article

Dual-functional pyrene implemented mesoporous silicon material used for the detection and adsorption of metal ions

Jing Huang, Honghui Cai, Qian Zhao, Yunpeng Zhou, Haibo Liu, Jing Wang *

School of Chemistry and Chemical Engineering, Guangxi University, Nanning 530004, China

ARTICLE INFO

Article history:
Received 18 September 2022
Received in revised form 17 January 2023
Accepted 30 January 2023
Available online 11 February 2023

Keywords:
Dual function
Nanomaterials
Mesoporous silica
Metal ions
Detection and adsorption

ABSTRACT

A fluorescent active organic–inorganic hybrid material PyN-SBA-15 was synthesized by implementing pyrene derivatives into mesoporous SBA-15 silica. PyN-SBA-15 had detection and removal functionalities toward Al^{3+}, Cu^{2+}, and Hg^{2+}. On the one hand, PyN-SBA-15 was used as a fluorescence sensor and displayed high sensitivity toward Al^{3+}, Cu^{2+}, and Hg^{2+} cations (limit of detection: 8.0×10^{-7}, 1.1×10^{-7}, and 2.9×10^{-6} mol·L^{-1}, respectively) among various analytes with "turn-off" response. On the other hand, the adsorption studies for these toxic analytes (Cu^{2+}, Hg^{2+}, and Al^{3+}) showed that the ion removal capacity could reach up to 45, 581, and 85 mg·g^{-1}, respectively. Moreover, the Langmuir isotherm models were better fitted with the adsorption data, indicating that the adsorption was mono-layer adsorption. Kinetic analysis revealed that the adsorption process was well described by the pseudo-second-order kinetic model for Cu^{2+} and Hg^{2+} and pseudo-first-order kinetic model for Al^{3+}. The prepared silica material could be reused in four recycles without significantly decreasing its adsorption capacity. Therefore, the PyN-SBA-15 material can serve as a promising candidate for the simultaneous rapid detection and efficient adsorption of metal ions.

1. Introduction

Clean water resources play an important role in the life activities of plants and animals. However, with the increase of human activities and rapid industrial development, metal ions in industrial wastewater will enter drinking water resources, causing water pollution and posing a threat to the health of living things [1–3]. As the most abundant metal element in the Earth's crust, aluminum (Al^{3+}) is widely distributed in the environment and is closely related to life activities [4]. However, excessive Al^{3+} in the environment will harm the normal growth of plants and the health of human beings [5,6]. Cu^{2+} is one of the trace elements necessary for various metabolic functions of living organisms. However, excessive amounts of Cu^{2+} can cause a range of diseases, such as cardiovascular disease and atherosclerosis [7]. Owing to the adverse effects of Cu^{2+}, the World Health Organization (WHO) set the maximum acceptable concentration of Cu^{2+} in drinking water to 2.0 mg·L^{-1} [8]. Heavy metal ions, such as mercury (Hg^{2+}), are one of the most harmful pollutants and tend to accumulate in the body, causing severe damage to mental and psychological health and even death in humans [9]. The US Environmental Protection Agency (EPA) has established a standard of 2×10^{-9} for the permissible level of inorganic Hg^{2+} ions in drinking water [10]. Therefore, the real-time detection and effective removal of excessive metal ions from industrial wastewater before discharging are important issues related to health and environmental safety [11].

Considerable efforts are accordingly being devoted to exploiting new technologies for sensing and adsorbing these toxic ions. In the past few decades, a series of organic probes and materials has been used for the selective and sensitive detection of metal ions [12–16]. However, the use of these probes is limited due to their complex synthesis, poor water solubility, and need for organic solvents. On the other hand, many types of nanomaterials have been developed as adsorbents for the removal of metal ions, such as covalent organic frameworks (COFs) [17], metal–organic frameworks (MOFs) [18], mesoporous silica materials [19], porous organic polymers (POPs) [20], and nanofibers [21]. However, most of the reported methods can only be used for the single detection or removal of metal ions, which limits their practical applications. To achieve the purpose of simultaneous detection and removal, some dual-functional materials, such as MOFs [22], cationic

* Corresponding author.
E-mail address: wjwyj82@gxu.edu.cn (J. Wang).

https://doi.org/10.1016/j.cjche.2023.01.014
1004-9541/

organic network [23], and magnetic nanoparticles [24], have also been exploited in recent years.

Recently, organic–inorganic hybrid materials have attracted extensive attention because of their tunable properties due to the combination of organic molecules and inorganic materials [25]. Among various hybrid materials, mesoporous silica (*e.g.*, SBA-15 [26]) exhibits excellent features such as high porosity, large specific surface area, orderly pore channels, and good stability. In addition, the abundance of hydroxyl groups on the surface of SBA-15 facilitates functionalization [27]. Through covalent bond connection, various fluorescent molecules could be grafted into porous SBA-15 material. Thus, functional SBA-15 shows excellent fluorescence detection performance while maintaining the ordered pore structure of mesoporous materials [28,29]. Moreover, the fascinating physical properties of SBA-15 make it an outstanding candidate material as a solid carrier with adsorption performance [30–32]. Therefore, SBA-15 is a potential mesoporous material that could be used for the simultaneous detection and adsorption of metal ions. Nevertheless, several studies have focused on the single detection or removal of metal ions. Hence, it is of great significance to develop the dual-functional advantages of SBA-15 for the simultaneous detection and removal of metal ions.

Considering the dual-functional possibilities of SBA-15 mesoporous material, we investigated the functionalized mesoporous silicon material for the rapid detection and efficient adsorption of metal ions. Herein, we conveniently constructed pyrene-derived ligand on the channel surface of SBA-15 mesoporous silica to obtain the hybrid material PyN-SBA-15, and studied its detection and adsorption capacity toward noxious metal ions. The research showed that PyN-SBA-15 exhibited extreme sensitivity and low detection limit for metal ions (Cu^{2+}, Hg^{2+} and Al^{3+}). The fluorescent ensemble of PyN-SBA-15, PyH-SBA-15, and PyU-SBA-15 was constructed to distinguish the metal ions of Cu^{2+}, Hg^{2+}, Al^{3+}, and Co^{2+}. Furthermore, PyN-SBA-15 showed high efficiency and recoverability in the removal of metal ions from an aqueous solution.

2. Experimental

2.1. Materials and instruments

SBA-15 was purchased from Nanjing XFNANO Materials Tech Co., Ltd. (China) and applied directly. 1-Pyrenecarboxaldehyde, formylhydrazine and 3-(aminopropyl) triethoxysilane (APTES) were purchased from Sigma-Aldrich (Shanghai, China) without further purification. Metal ions solutions are prepared from their chlorides. Analyze pure levels of solvents, *i.e.*, ethanol (EtOH), toluene and chloroform ($CHCl_3$) were purchased from commercial suppliers.

2.2. Instruments

The small angle X-ray powder diffraction (SXRD) pattern was obtained on a Smartlab9K diffractometer (Rigaku, Japan) with Cu K_α radiation. Transmission electron microscopy (TEM) images carried out using JEM-2100F microscope (JEOL, Japan). The thermogravimetric analysis (TGA) was measured using a STA449-F5 TAQ600 instrument (Netzsch, Germany) at a 10 °C·min^{-1} heating rate. Micrometrics ASAP 2460 instrument (Micrometrics, USA) was used to measure the nitrogen adsorption–desorption isotherms. The Fourier transform infrared (FT-IR) were recorded on 660-IR (ATR) FT-IR spectrophotometer (Varian, USA). Fluorescence spectra were examined by 960 MC spectroscopy (Shanghai Lengguang Technology Co., Ltd., China), with an excitation wavelength of 368 nm. Nuclear magnetic resonance (^{1}H NMR) spectra was taken on a 600 MHz Bruker spectrometer with TMS as an internal standard. Mass spectra were tested on the Avance III HD500 instrument (Bruker, Germany). To determine metal ion concentrations, inductively coupled plasma optical emission spectrometer (ICP-OES) analyses were performed on the Thermo instrument (ICAP7000, Thermo Scientific, USA).

2.3. Synthesis and characterization of PyN-SBA-15

Synthesis of PYF. 0.35 mmol (0.0805 g) of 1-pyrenecarboxaldehyde and excess formylhydrazine (0.70 mmol, 0.42 g) were dissolved in 50 ml of ethanol, stirring for 30 h at room temperature. After atmospheric filtration, the crude product was cleaned with ethanol several times to obtain pure (pyren-1-ylmethylene)formohydrazide (abbreviated as PYF) (Fig. 1). Mass spectra: m/z $[M + H]^+$ calculated: 273.0, found: 273.1 (Fig. S1 in Supplementary Material). ^{1}H NMR (500 MHz, DMSO-d_6) δ 9.93 (s, 1H), 9.29 (d, J = 9.4 Hz, 1H), 8.85 (d, J = 8.1 Hz, 1H), 8.45 (ddd, J = 11.3, 7.8, 3.3 Hz, 5H), 8.36 (s, 1H), 8.31 (d, J = 8.9 Hz, 1H), 8.18 (d, J = 7.7 Hz, 1H), 5.76 (s, 1H) (Fig. S2).

Synthesis of PyN-SBA-15. The synthesis of APTES-SBA-15 was based on the method described in the literature previously reported by our group (Fig. 1) [33]. Whereafter, 0.4 g APTES-SBA-15 was weighed and stirred in 30 ml toluene for 10 min, then 1 mmol (0.272 g) of PYF was added to the mixture, and refluxed for 24 h at 110 °C. The product was cleaned with $CHCl_3$ and centrifuged to remove excess PYF. PyN-SBA-15 was obtained after drying at 80 °C. Compared with TGA curve of the original SBA-15 [34], the amount of organic part (functional group, $C_{21}H_{18}N_3$, MW: 312 g·mol^{-1}) of PyN-SBA-15 is 22.83% (mass). Therefore the moles of organic groups per gram of SBA-15 is calculated to 22.83%/312 = 0.73 mmol. Namely, the amount of functional group in SBA-15 is 0.73 mmol·g^{-1} (Fig. S3).

2.4. Fluorescence studies

For fluorescence studies, 0.5 ml of PyN-SBA-15 suspension (0.5 g·L^{-1}, suspended in aqueous medium) was mixed with various analytes in aqueous buffer solution individually and sonicated for 20 min. The obtained suspension mixtures were allowed to stand at room temperature for 12 h before fluorescence measurement. This process was repeated before each fluorescence measurement. The fluorescence measurements were carried out by using an excitation wavelength at 368 nm.

2.5. Adsorption of metal ions

Adsorption experiments were carried out in an aqueous system at room temperature to determine adsorption parameters, such as adsorption isotherms and kinetic models. In a typical experiment, 5 mg of PyN-SBA-15 was added to 10 ml aqueous solutions containing different concentrations of metal ions (*i.e.*, 10–100 mg•L^{-1} Cu^{2+}, Al^{3+} and 20–600 mg·L^{-1} Hg^{2+}). Then the mixtures were stirred for 12 h at room temperature to ensure that the adsorption reaches equilibrium, centrifuged and filtered with 0.45 μm membrane. The final concentration of various metal ions was measured by ICP-OES. The equilibrium adsorption capacity is calculated using the equation.

$$q_e = (C_0 - C_e)V/m \quad (1)$$

where q_e (mg·g^{-1}) is the equilibrium adsorption capacity, C_0 and C_e (mg·L^{-1}) are the initial and final concentration of metal ions in an aqueous solution, V is the volume of the solution (L), and m is the mass of the material (g).

The adsorption isotherms were analyzed with the Langmuir and Freundlich isotherm model. The Langmuir isotherm model applies

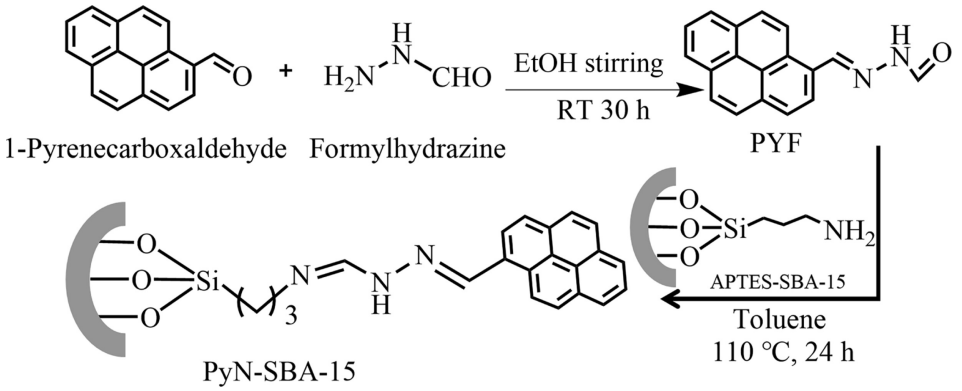

Fig. 1. Schematic illustration of the procedure for the preparation of PYF and PyN-SBA-15.

to monolayer adsorption, whereas the Freundlich isotherm model describes heterogeneous surfaces.

$$\text{Langmuir model}: C_e/q_e = C_e/q_{max} + 1/(q_{max} \cdot K_L) \quad (2)$$

$$\text{Freundlich model}: \ln q_e = \ln K_F + \frac{1}{n} \ln C_e \quad (3)$$

where q_e and q_{max} ($mg \cdot g^{-1}$) are the equilibrium adsorption capacity and the maximum adsorption capacity, respectively. C_e ($mg \cdot L^{-1}$) is the equilibrium metal concentrations. K_L ($L \cdot mg^{-1}$) is the Langmuir adsorption constant. K_F is the Freundlich constant related to the adsorption capacity of the adsorbent and n is a heterogeneity parameter of the adsorbent surface. Langmuir equation separation factor (R_L) is defined as $R_L = 1/(1 + K_L C_0)$. Where, K_L is the Langmuir adsorption isothermal constant, C_0 is the initial concentration of metal ions, when $R_L > 1$, the adsorption system is considered inappropriate, $0 < R_L < 1$, the adsorption system is appropriate, when $R_L = 1$, the adsorption system is linear, $R_L = 0$, the adsorption system is irreversible.

Kinetic studies for Al^{3+}, Cu^{2+} and Hg^{2+} were conducted to determine the kinetic model. The process was as follows: 5 mg of sorbent PyN-SBA-15 were dispersed in 10 ml Al^{3+}, Cu^{2+} or Hg^{2+} solution with the same initial concentration (100 $mg \cdot L^{-1}$). Each of the mixtures was continuously stirred for 15, 30, 60, 90, 120, 180 min at room temperature. The analyte concentrations in the filtrate were analyzed by ICP-OES for kinetic models. Two kinetic models, *i.e.*, the pseudo-first-order and pseudo-second-order which can be expressed as Eqs. (4) and (5), respectively.

$$\text{Pseudo-first-order kinetic model}: \frac{1}{q_t} = \frac{K_1}{q_e t} + \frac{1}{q_e} \quad (4)$$

$$\text{Pseudo-second-order kinetic model}: \frac{t}{q_t} = \frac{1}{K_2 q_e^2} + \frac{1}{q_t} \quad (5)$$

where q_t and q_e ($mg \cdot g^{-1}$) are the amounts of adsorbed at time t and at equilibrium, respectively. K_1 (min^{-1}) and K_2 ($g \cdot mg^{-1} \cdot min^{-1}$) are the rate constants for the pseudo-first-order constant and pseudo-second-order model, respectively.

2.6. The calculation of limit of detection (LOD) and quenching constant (K_{SV})

The calculation of theoretical detection limit according to the equation LOD = $3\sigma/k$, where σ is standard deviation of blank solutions of PyN-SBA-15 measured by ten times, and k is the slope of fluorescence intensity *versus* [M^{n+}] plot. A linear quenching equation $F_0/F = K_{SV}[m] + 1$ and exponential quenching equation $F_0/F = A \cdot e^{K_{SV}[m]} + B$ were used to fit the linear and nonlinear Stern–Volmer curve and calculate the quenching constant (K_{SV}) of PyN-SBA-15 toward M^{n+}. In this equation, F_0 is the initial fluorescence intensity of the PyN-SBA-15, F is the fluorescence intensity of PyN-SBA-15 after addition of M^{n+}, [m] is the concentration of M^{n+}.

3. Results and Discussion

The chemical structures of three organic–inorganic hybrid materials, namely, PyN-SBA-15, PyU-SBA-15, and PyH-SBA-15, and their corresponding solid-state images are shown in Fig. 2. As for the organic part of these three materials, the fluorophores were pyrene. The solid-state fluorescent colors varied by changing the metal coordination groups. Specifically, PyN-SBA-15, PyU-SBA-15, and PyH-SBA-15 showed yellow, yellow-green, and blue color, respectively, under 365 nm UV light irradiation. The synthetic scheme and procedures of PyN-SBA-15 are given in Fig. 1 and Section 2.3, respectively. The detailed synthetic procedures and characterizations of PyU-SBA-15 and PyH-SBA-15 had been reported in our previous research [33,35].

3.1. Characterization of PyN-SBA-15

Fig. 3(a) shows the SXRD pattern of PyN-SBA-15. Three typically distinct reflections are (1 0 0), (1 1 0), and (2 0 0) planes, revealing a hexagonal mesoscopic organization which was consistent with the original SBA-15 [34,36]. The TEM image of PyN-SBA-15 clearly showed the well-ordered silica walls with pores (Fig. S4), demonstrating that the functionalized mesoporous silicon material still preserved the structures of original SBA-15 [34]. The N_2 adsorption–desorption isotherms of SBA-15 and PyN-SBA-15 displayed a typical type IV isotherm (Fig. 3(b)), with clear H1 hysteresis loop at higher relative pressure, which is the prototypical property of mesoporous materials [37]. Moreover, compared with SBA-15, the surface area, pore size, and pore volume of PyN-SBA-15 decreased (Table S1).

Fig. 4 displays the FT-IR spectra of SBA-15, PYF, and PyN-SBA-15. For SBA-15 and PyN-SBA-15, the peak around 3437 cm^{-1} could be attributed to the typical stretching vibrations of Si—OH [34]. The peak at 805 cm^{-1} was caused by the asymmetric stretching vibration of Si—OH. Two apparent bands at 467 and 1081 cm^{-1} were associated with the stretching and bending vibrations of Si—O—Si, and the peak at 1630 cm^{-1} was caused by the physical water absorption of the material. And the peak at 3037 cm^{-1} was attributed to the unsaturated alkane peaks (=C—H) on pyrene [34]. Compared with SBA-15, in the spectra of PyN-SBA-15, the additional peaks at 692, 1564, and 1631 cm^{-1} were attributed to the N—H stretching and bending vibrations, the band at 1474 cm^{-1} was due to the C—N vibration of alkyl amine, and the peaks at

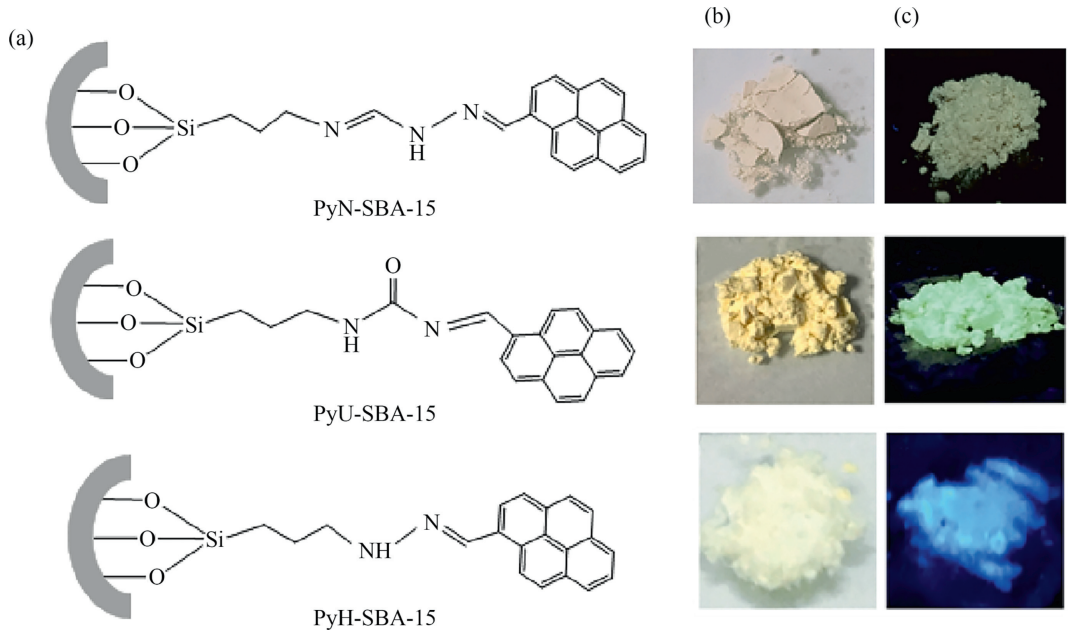

Fig. 2. Chemical structures (a) and solid-state photographs of PyN-SBA-15, PyU-SBA-15, and PyH-SBA-15 under day light (b) and 365 nm UV light irradiation (c).

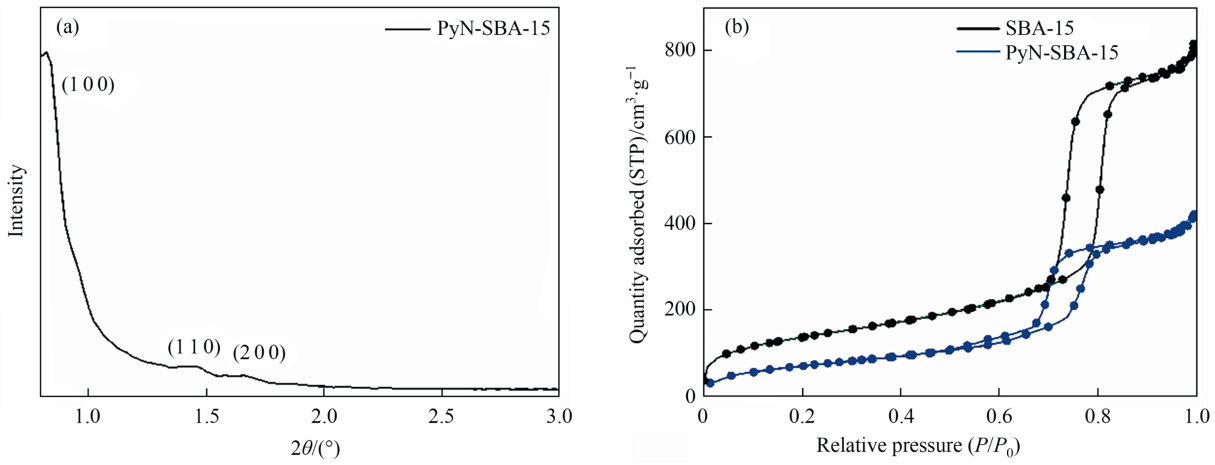

Fig. 3. (a) SXRD pattern and (b) N_2 adsorption–desorption isotherms of PyN-SBA-15.

2922 and 2851 cm^{-1} were attributed to the saturated alkane peaks (C—H) on APTES. The presence of all characteristic peaks in the spectra of PyN-SBA-15 indicated that PYF was successfully grafted and cleaned. These results indicated that the pyrene fluorophore and nitrogenous and carbonaceous functional groups had been successfully grafted onto the channel of SBA-15 and that the mesoporous structure was well preserved.

3.2. . Optimization of application conditions

The normalized emission spectra of PyN-SBA-15 showed monomer emission of pyrene at 383 and 399 nm and excimer emission of pyrene at 474 nm. To better present the spectral information, the excitation wavelength of 368 nm was used for the following studies (Fig. 5).

To ensure the stability of PyN-SBA-15 during the fluorescence detection, the detection conditions, such as time and pH values, were studied. pH had an obvious effect on the fluorescence of PyN-SBA-15, and the fluorescence intensity at 383 and 474 nm was relatively stable in the pH range of 6.0–11.0 (Fig. S5). The emission peak at 474 nm increased as a function of time, which could be attributed to the aggregation of pyrene fluorophore within the limited mesopores. However, the monomer emission of pyrene at 383 and 399 nm was almost unaffected by time. Thus, the time of 12 h and pH of 6.0 were used for the subsequent experiments, unless otherwise stated.

3.3. Sensing studies

As shown in Fig. 6, the fluorescent response of PyN-SBA-15 toward metal ions was studied in aqueous solution (HEPES buffer, pH = 6.0). Among 12 kinds of investigated metal ions, the fluorescence of PyN-SBA-15 displayed minimal or almost no changes in the presence of Na^+, K^+, Mg^{2+}, Ca^{2+} and Ba^{2+}; the monomer emission peaks of pyrene at 383 and 399 nm quenched to varying degrees in the presence of Ni^{2+}, Cd^{2+}, Zn^{2+} and Co^{2+}; whereas the two monomer peaks dramatically quenched in the presence of Al^{3+}, Cu^{2+}, and Hg^{2+}. Moreover, the fluorescence quenching of PyN-SBA-15 by Al^{3+}, Cu^{2+}, and Hg^{2+} was investigated in the presence of competitive metal ions (Figs. S6 and S7). The fluorescent

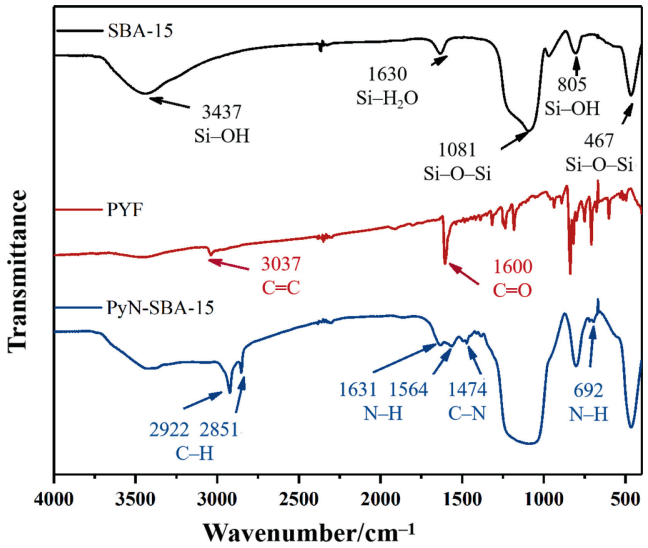

Fig. 4. FT-IR spectra of SBA-15, PYF, and PyN-SBA-15.

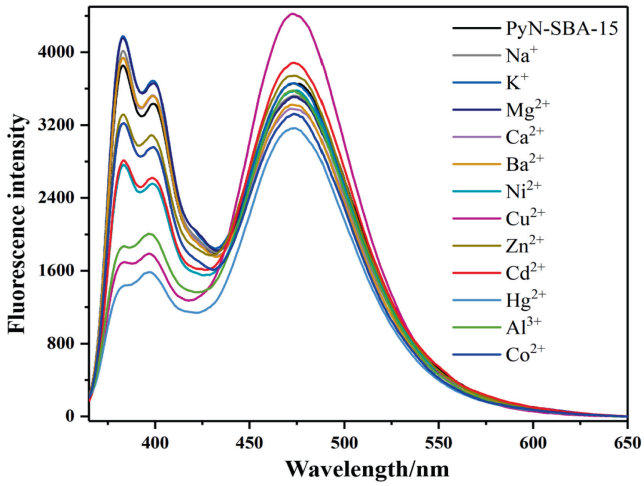

Fig. 6. Fluorescence spectra of PyN-SBA-15 (0.05 g·L^{-1}) in the presence of various metal ions (1.0×10^{-4} mol·L^{-1}) in the aqueous solution (20 mmol·L^{-1} HEPES buffer, pH = 6.0).

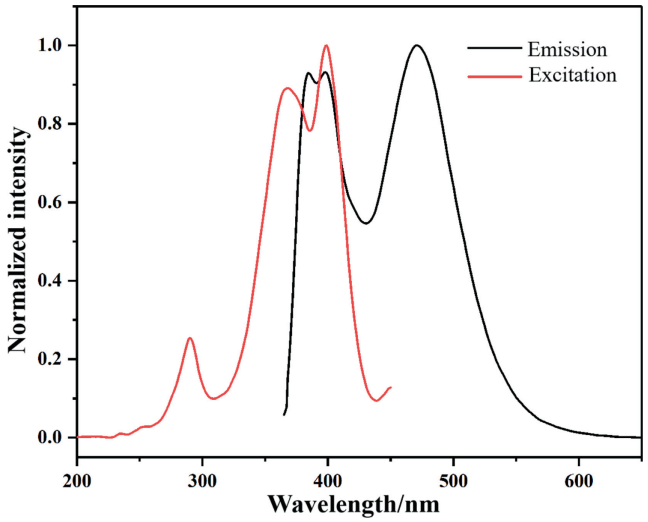

Fig. 5. Normalized emission and excitation spectra of PyN-SBA-15 (0.05 g·L^{-1}) in aqueous solution (20 mmol·L^{-1} HEPES buffer, pH = 6.0).

changes (F/F_0) of PyN-SBA-15 by Al^{3+}, Cu^{2+}, and Hg^{2+} changed in the presence of 3.0 equiv. other ions, some F/F_0 even changed to be more than 1.3 (Fig. S6). While the fluorescence quenching of PyN-SBA-15 by Al^{3+}, Cu^{2+}, and Hg^{2+} was not affected in the presence of 2.0 equiv. competitive metal ions (Fig. S7), indicating that this material has a good anti-interference performance in response to Al^{3+}, Cu^{2+}, and Hg^{2+} metal ions, when the concentration of the interfering substances was below 2.0 equiv. [38–40]. Then, the titration experiments of PyN-SBA-15 toward different concentrations of Al^{3+}, Cu^{2+}, and Hg^{2+} were carried out to determine the limit of detection (LOD) and Stern–Volmer quenching constants (K_{sv}) of the three kinds of metal ions.

As shown in Fig. 7(a), the fluorescence intensity of PyN-SBA-15 at 383 nm gradually decreased with increasing Al^{3+} concentration. When the Al^{3+} concentration ranged from 0 to 4.0×10^{-5} mol·L^{-1}, the fluorescence intensity at 383 nm *versus* the concentration of Al^{3+} showed a good linear relationship (Fig. 7(b)). The same phenomena were also observed for the titration of Hg^{2+} and Cu^{2+} (Figs. S8 and S9). The LODs of three metal ions were calculated to be 8.0×10^{-7} mol·L^{-1} (Al^{3+}), 1.1×10^{-7} mol·L^{-1} (Cu^{2+}), and 2.9×10^{-6} mol·L^{-1} (Hg^{2+}). In addition, the Stern–Volmer (SV) plot for Al^{3+} was nonlinear (Fig. 7(c)), whereas linear Stern–Volmer plots were observed for Cu^{2+} and Hg^{2+} (Fig. S10). A positive deviation of the SV plot from linearity indicated that the quenching mechanism for Al^{3+} was either static or a combination of static and dynamic. A linear fitting for $Cu^{2+}$and Hg^{2+} suggests a static mechanism. The K_{sv} values were calculated, and the results are shown in Table 1. The nonlinear K_{sv} for Al^{3+} was found to be 2.4×10^4 L·mol^{-1}, and the linear K_{sv} for Cu^{2+} and Hg^{2+} were calculated to be 1.2×10^5 and 7.1×10^3 L·mol^{-1}, respectively.

As shown in Fig. 8, the organic functionalized mesoporous silicon exhibited different response ability to metal ions by retaining the pyrene fluorophore in the organic function, but varying the metal ion coordination groups. As stated above, PyN-SBA-15 could respond to three kinds of metal ions (Al^{3+}, Cu^{2+} and Hg^{2+}). However, it is difficult to distinguish the three metal ions through fluorescent response of PyN-SBA-15. Similar to PyN-SBA-15, PyH-SBA-15 was sensitive to Cu^{2+}, Hg^{2+}, and Co^{2+}, but did not have the ability to distinguish between them [34]. Conversely, PyU-SBA-15 exhibited excellent selectivity toward Hg^{2+} by introducing carbonyl group as an additional metal coordination site [37].

To recognize various metal ions selectively and sensitively, a fluorescent sensor ensemble composed of PyN-SBA-15, PyH-SBA-15, and PyU-SBA-15 was constructed (Fig. 9). In the first channel, PyU-SBA-15 could selectively recognize Hg^{2+} through the "turn-off" fluorescent signals; in the second channel, PyN-SBA-15 could differentiate the metal ions into two groups. On the one hand, "turn-off" fluorescent signals were observed toward Cu^{2+} and Al^{3+}. On the other hand, no fluorescent signal was observed toward Co^{2+}. In the third channel, PyH-SBA-15 distinguished Cu^{2+} and Al^{3+} by monitoring the fluorescent signals of "turn-off" and "no response," respectively.

3.4. Adsorption studies

3.4.1. Adsorption isotherm

Materials with high detection and adsorption performance of hazardous species are of great importance. Considering that functionalized mesoporous materials are rich in nitrogen-based ligands and can effectively bind with metal ions, PyN-SBA-15 may be used for metal ion removal. Thus, a series of adsorption experiments including the adsorption isotherm and the adsorption kinetic

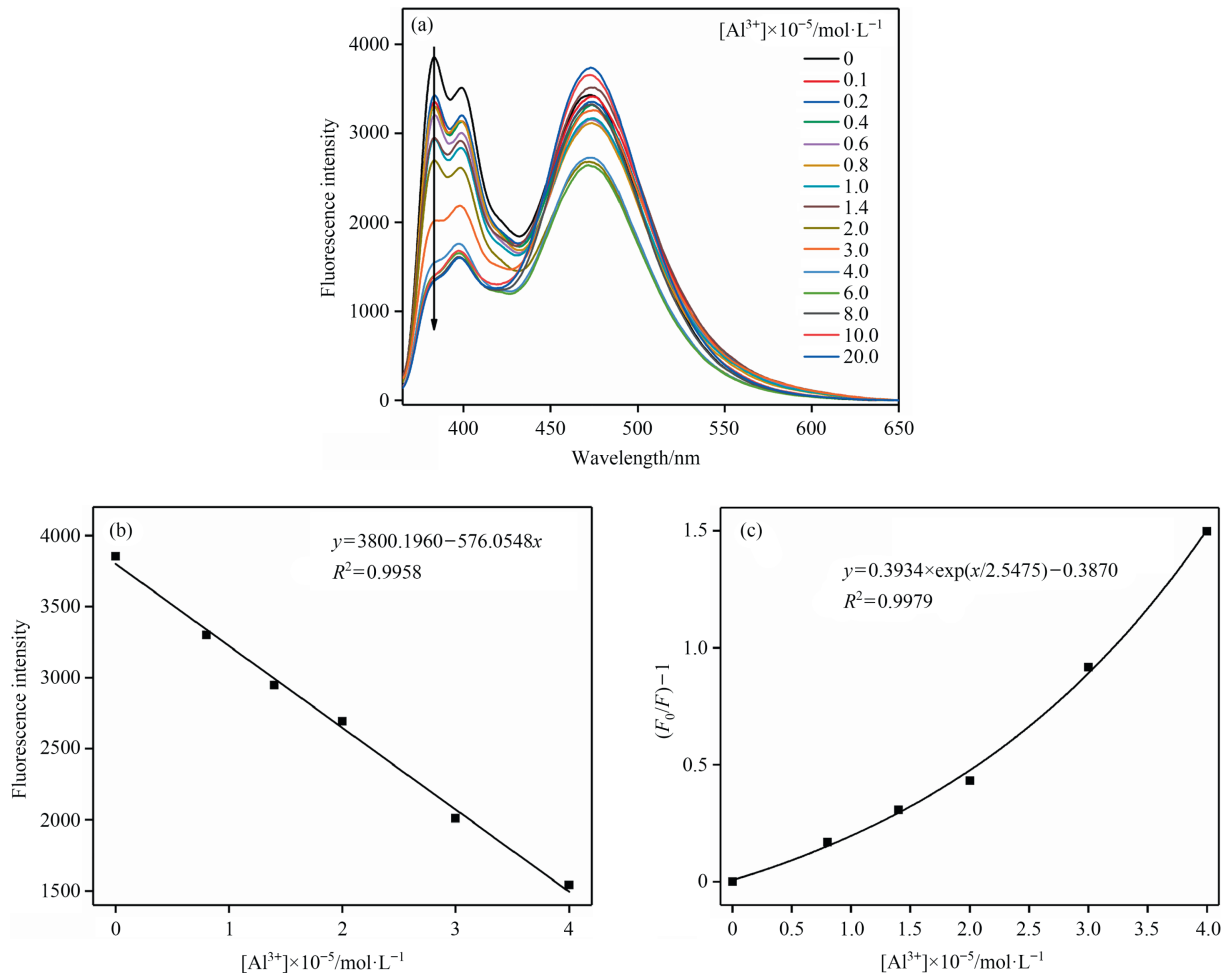

Fig. 7. (a) Fluorescence spectra of PyN-SBA-15 (0.05 g·L^{-1}) in the presence of different concentrations of Al^{3+} in aqueous solution (HEPES buffer, 20 mmol·L^{-1}, pH = 6.0) (λ_{ex} = 368 nm). (b) Fluorescence intensity of PyN-SBA-15 (0.05 g·L^{-1}) at 383 nm *versus* the concentration Al^{3+}. (c) Nonlinear Stern–Volmer plot for Al^{3+}.

Table 1
Detection linear range, LOD, and K_{sv} of PyN-SBA-15 toward metal ions

Metal ions	Linear range/mol·L^{-1}	LOD/mol·L^{-1}	K_{sv}/L·mol^{-1}
Al^{3+}	0–4.0 × 10^{-5}	8.0 × 10^{-7}	1.4 × 10^{5}
Cu^{2+}	0–2.0 × 10^{-6}	1.1 × 10^{-7}	1.2 × 10^{5}
Hg^{2+}	0–4.0 × 10^{-5}	2.9 × 10^{-6}	7.1 × 10^{3}

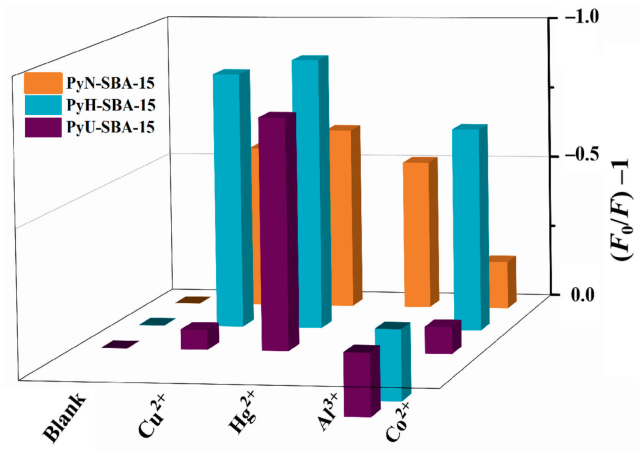

Fig. 8. Relative emission intensity of PyN-SBA-15, PyH-SBA-15, and PyU-SBA-15 to various metal ions (1.0 × 10^{-4} mol·L^{-1}).

studies was carried out at room temperature to evaluate the adsorption capacity of metal ions.

To evaluate the maximum adsorption capacity for metal ions, adsorption isotherm studies were carried out, and the equilibrium adsorption capacity was calculated according to the equation $q=(C_0-C)V/m$. As shown in Fig. 10, the adsorption capacity of Al^{3+}, Cu^{2+}, and Hg^{2+} increased with increasing equilibrium concentration, and the maximum adsorption capacities measured in the experiments were 85, 45, and 581 mg·g^{-1}, respectively. Langmuir and Freundlich models were used to analyze the adsorption isotherms of the three metal ions, and the isotherm parameters are compared in Table 2. The correlation coefficient obtained by the Langmuir model was higher than that of the Freundlich model, which indicated that the adsorption of the three metal ions on PyN-SBA-15 was monolayer adsorption. The maximum fitting adsorption capacities of Al^{3+}, Cu^{2+}, and Hg^{2+} were 257, 87, and 1245 mg·g^{-1}, respectively. The adsorption R_L values of the three metal ions were all between 0 and 1, concluding that the adsorbent has good adsorption performance for Al^{3+}, Cu^{2+}, and Hg^{2+}.

3.4.2. Adsorption kinetics

Then, the influence of contact time on the adsorption of PyN-SBA-15 toward metal ions was studied to investigate the kinetic behavior. The initial concentration of metal ions was 100 mg·L^{-1}, and the adsorbent dosage was 5 mg. As shown in Fig. S11, the concentration of metal ions decreased significantly in the first 15 min due to the abundant adsorption sites on PyN-SBA-15 at the

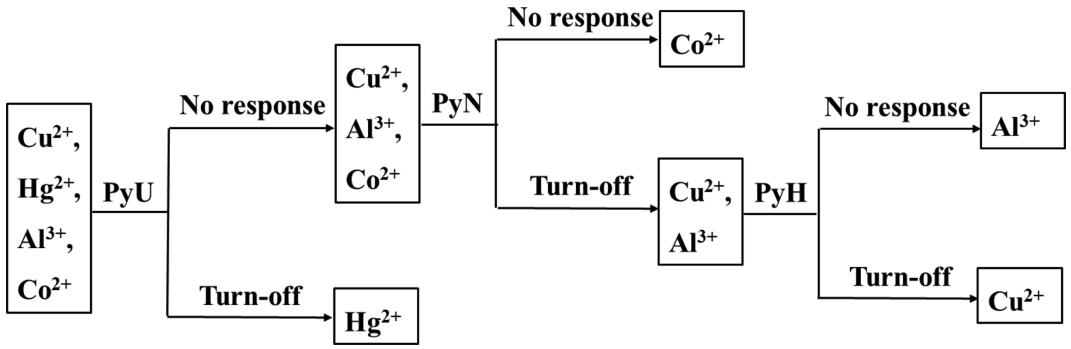

Fig. 9. Discrimination of four metal ions by PyU-SBA-15, PyN-SBA-15, and PyH-SBA-15.

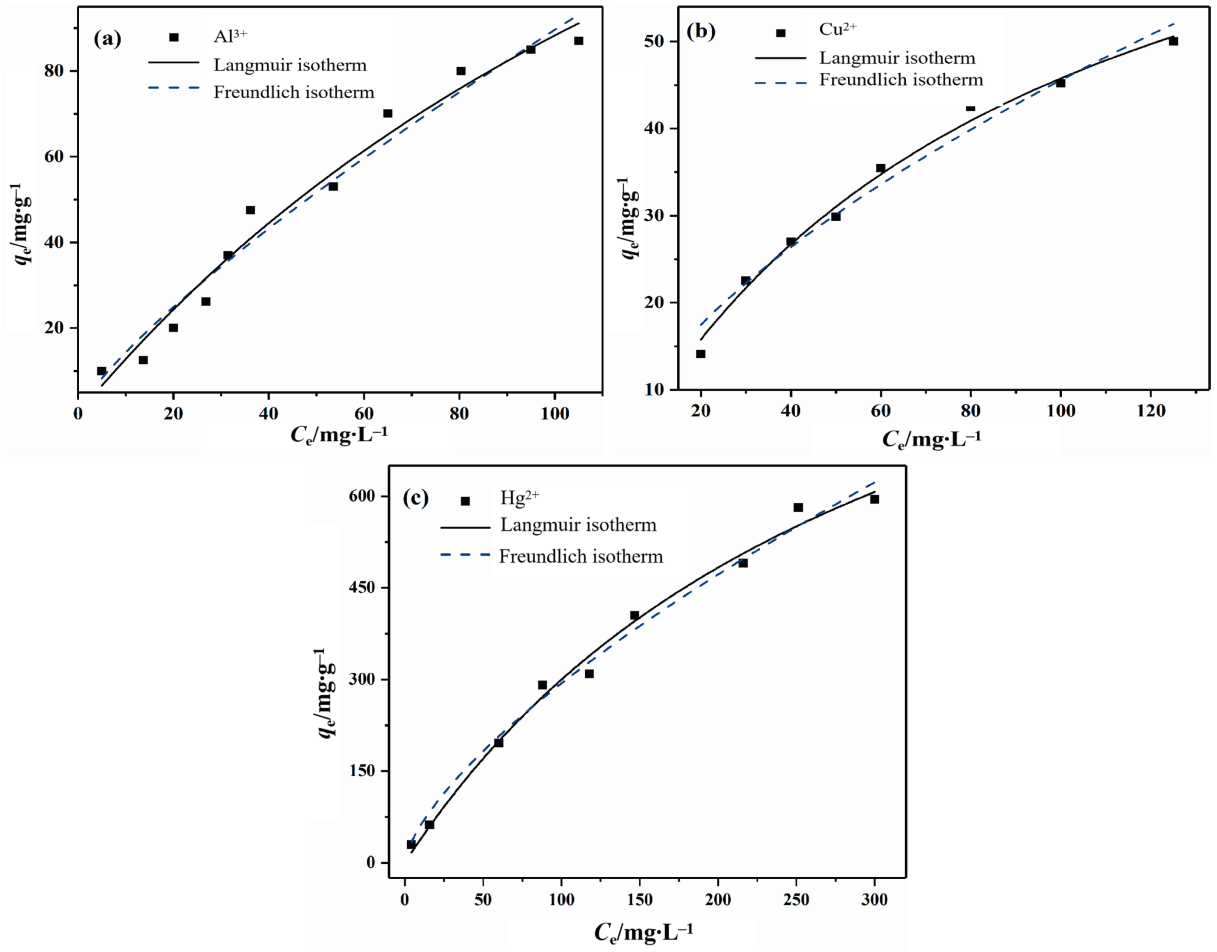

Fig. 10. Adsorption isotherms of PyN-SBA-15 material toward (a) Al^{3+}, (b) Cu^{2+}, and (c) Hg^{2+}.

Table 2
Langmuir and Freundlich adsorption parameters for metal ions

Metal ions	Exptl. q_{max}/mg·g^{-1}	Langmuir isotherm			Freundlich isotherm		
		q_{max} /mg·g^{-1}	K_L/L·mg^{-1}	R^2	K_F	n	R^2
Al^{3+}	85	257	0.0052	0.9771	2.2964	1.2569	0.9698
Cu^{2+}	45	87	0.0110	0.9917	2.9328	1.6790	0.9746
Hg^{2+}	581	1245	0.0032	0.9921	12.5772	1.4617	0.9894

beginning of adsorption, which could rapidly combine with metal ions. The adsorption reached equilibrium about 3, 3 and 2 h for Al^{3+}, Cu^{2+} and Hg^{2+}, and PyN-SBA-15 achieved the best adsorption toward Hg^{2+} with a removal rate of up to 82%.

The quasi-first-order and quasi-second-order kinetic models were used to further analyze the adsorption kinetics. The fitting results were shown in Fig. 11, and the kinetic constant K and linear correlation coefficient R^2 are shown in Table 3. The pseudo-first-

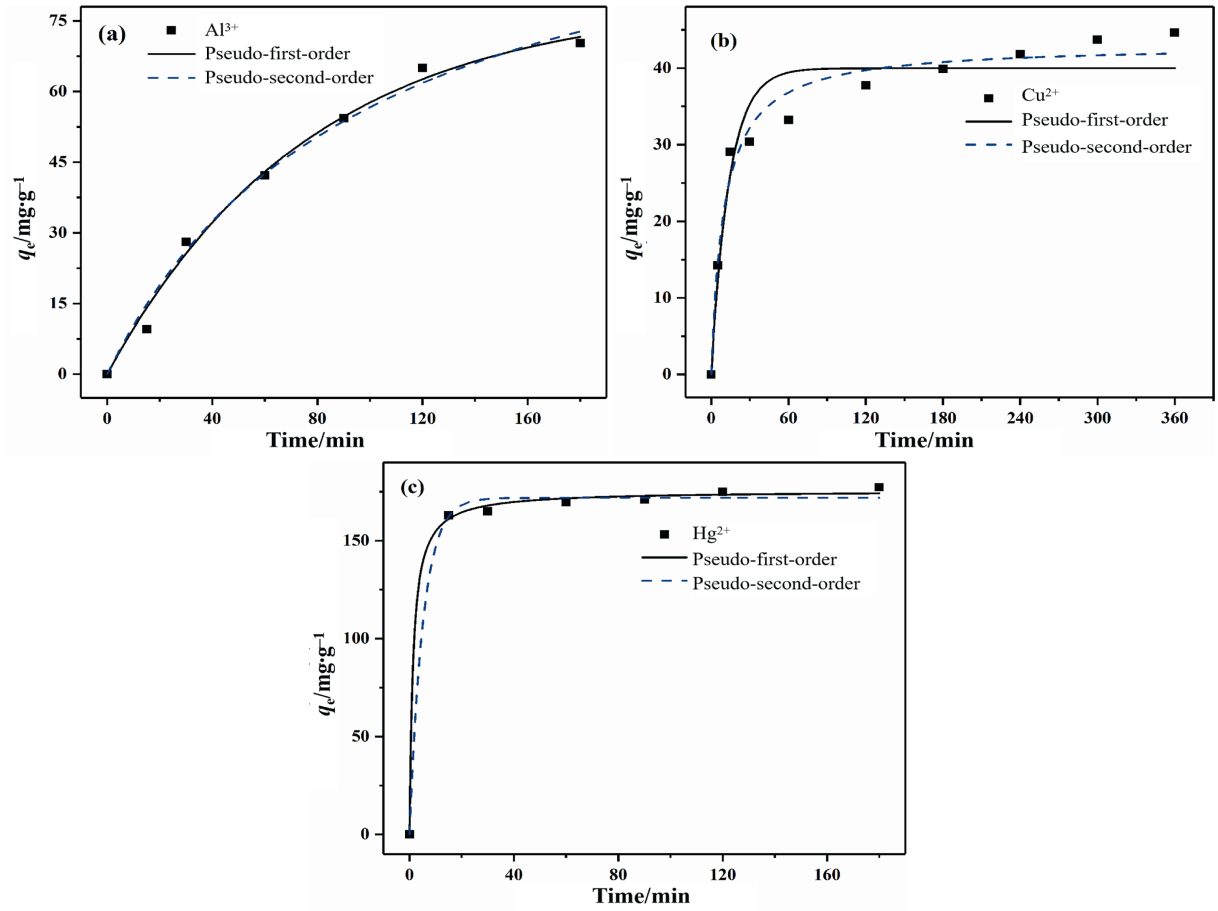

Fig. 11. Adsorption kinetic curves of (a) Al^{3+}, (b) Cu^{2+}, and (c) Hg^{2+} by pseudo-first-order model and pseudo-second-order model.

Table 3
Kinetic parameters for Al^{3+}, Cu^{2+}, and Hg^{2+} adsorption onto PyN-SBA-15

Metal ion	Exptl. q_e /mg·g^{-1}	Pseudo-first-model			Pseudo-second-model		
		K_1/min^{-1}	q_e/mg·g^{-1}	R^2	K_2/g·mg^{-1}·min^{-1}	q_e/mg·g^{-1}	R^2
Al^{3+}	72	0.0130	79	0.9920	0.000089	112	0.9887
Cu^{2+}	45	0.0711	39	0.9350	0.002280	43	0.9758
Hg^{2+}	175	0.1925	171	0.9695	0.004250	175	0.9987

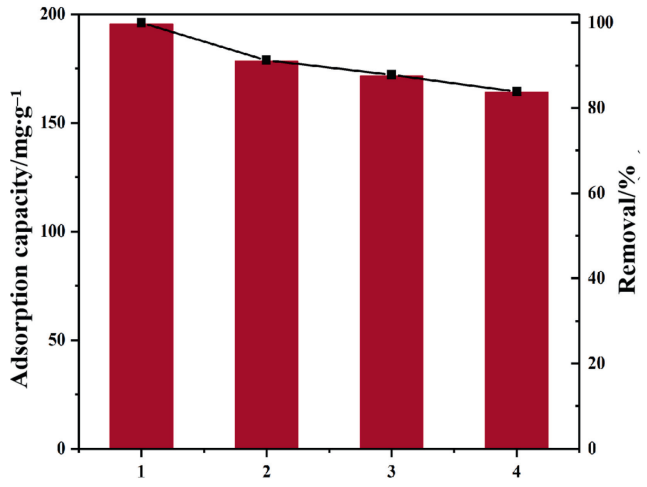

Fig. 12. Effect of recycling times on the adsorption capability of PyN-SBA-15 for Hg^{2+}.

order correlation coefficient (R^2 = 0.9920) of PyN-SBA-15 for Al^{3+} was greater than the pseudo-second-order correlation coefficient (R^2 = 0.9887), indicating that the adsorption process was mainly physical adsorption, whereas the adsorption process of Cu^{2+} and Hg^{2+} was more in line with the second-order kinetic model, indicating that the adsorption process was mainly chemical adsorption. Adsorption is controlled by the chemical interaction of electron sharing or transfer between adsorbent and adsorbate. The kinetic constants in the table indicate that the adsorption rate of Hg^{2+} is the fastest.

3.5. Recyclability study

The reproducibility of materials is one of the important factors that evaluate the material economy. Therefore, recycling experiments were carried out to evaluate the material reusability. Hg^{2+} was selected to conduct four cycles of adsorption–desorption experiments due to its good adsorption performance on PyN-SBA-15. During the desorption process, PyN-SBA-15 was recycled

by using 0.1 mol·L^{-1} EDTA and deionized water as desorption medium. The results showed a slight decrease in the adsorption capacity and removal rate after four cycles (Fig. 12). Good recyclability suggests that PyN-SBA-15 has the potential to be an economical and stable adsorbent for adsorbing metal ions from water. In addition, the detection and adsorption of metal ions by PyN-SBA-15 was compared with other nanomaterials. As can be seen from Table S2, compared to most of the reported materials, PyN-SBA-15 exhibits good performance: (1) PyN-SBA-15 can achieve dual detection and adsorption abilities toward three metal ions; (2) comparable detection limits; (3) higher Hg^{2+} adsorption capacity.

4. Conclusions

In summary, an organic functionalized mesoporous silica material, namely, PyN-SBA-15, with fluorescence activity was prepared by combining pyrene ligand PYF with mesoporous silica SBA-15. PyN-SBA-15 realized dual functions of detection and removal of Al^{3+}, Cu^{2+}, and Hg^{2+}. PyN-SBA-15 responded to Al^{3+}, Cu^{2+}, and Hg^{2+} ions with "turn-off" fluorescence signals and could achieve the quantitative detection of Al^{3+}, Cu^{2+}, and Hg^{2+} with low LODs of 8.0×10^{-7}, 1.1×10^{-7}, and 2.9×10^{-6} mol·L^{-1}, respectively. The adsorption of Al^{3+}, Cu^{2+}, and Hg^{2+} on PyN-SBA-15 accorded with the Langmuir adsorption model and had higher saturated adsorption capacity (q_{max} = 257, 87, and 1245 mg·g^{-1}, respectively) and faster adsorption kinetics. In addition, PyN-SBA-15 exhibited prominent adsorption and recycling performance after four adsorption–desorption cycles, making it an excellent adsorbent for the removal of metal ions.

Data Availability

No data was used for the research described in the article.

Declaration of Competing Interest

The authors declare that they have no known competing financial interests or personal relationships that could have appeared to influence the work reported in this paper.

Acknowledgements

This work was supported by the National Natural Science Foundation of China (21966006).

Supplementary Material

Supplementary data to this article can be found online at https://doi.org/10.1016/j.cjche.2023.01.014.

References

[1] H.B. Wan, Q.F. Xu, P.Y. Gu, H. Li, D.Y. Chen, N.J. Li, J.H. He, J.M. Lu, AIE-based fluorescent sensors for low concentration toxic ion detection in water, *J. Hazard. Mater.* 403 (2021) 123656.
[2] J. Li, X.X. Wang, G.X. Zhao, C.L. Chen, Z.F. Chai, A. Alsaedi, T. Hayat, X.K. Wang, Metal–organic framework-based materials: Superior adsorbents for the capture of toxic and radioactive metal ions, *Chem. Soc. Rev.* 47 (7) (2018) 2322–2356.
[3] E. Da'na, Adsorption of heavy metals on functionalized-mesoporous silica: A review, *Micropor. Mesopor. Mater.* 247 (2017) 145–157.
[4] B. Kaur, N. Kaur, S. Kumar, Colorimetric metal ion sensors—A comprehensive review of the years 2011–2016, *Coord. Chem. Rev.* 358 (2018) 13–69.
[5] J. Liang, H.B. Liu, J. Wang, Pyrene-based ratiometric and fluorescent sensor for selective Al^{3+} detection, *Inorg. Chim. Acta* 489 (2019) 61–66.
[6] C. Rodrigues, F.R. Lapolli, I. Padilla, A. López-Delgado, Highly efficient removal of aluminum, iron, and manganese ions using Linde type-A zeolite obtained from hazardous waste, *Chemosphere* 267 (2021) 128919.
[7] J. Wang, J. Liang, X. Liu, H. Xiao, F.P. Dong, Y.L. Wang, X. Shu, F.R. Huang, H.B. Liu, Thiazoline-pyrene selective and sensitive fluorescence turn-on sensor for detection of Cu^{2+}, *Spectrochim. Acta A* 215 (2019) 260–265.
[8] J.Y. Lee, C.H. Chen, S. Cheng, H.Y. Li, Adsorption of Pb(II) and Cu(II) metal ions on functionalized large-pore mesoporous silica, *Int. J. Environ. Sci. Technol.* 13 (1) (2016) 65–76.
[9] L.H. Zhi, W. Zuo, F.J. Chen, B.D. Wang, 3D MoS_2 composition aerogels as chemosensors and adsorbents for colorimetric detection and high-capacity adsorption of Hg^{2+}, *ACS Sustain. Chem. Eng.* 4 (6) (2016) 3398–3408.
[10] EPA (US Environmental Protection Agency) established the mercury (II) limit on 2 ppb, EPA-HQ-OPPT-2005-0013, 2006.
[11] X.L. Liu, R. Ma, X.X. Wang, Y. Ma, Y.P. Yang, L. Zhuang, S. Zhang, R. Jehan, J.R. Chen, X.K. Wang, Graphene oxide-based materials for efficient removal of heavy metal ions from aqueous solution: A review, *Environ. Pollut.* 252 (2019) 62–73.
[12] Y.X. Li, J.Z. Hou, H.P. Zhou, M.Q. Jia, S.S. Chen, H. Huang, L. Zhang, C. Yu, A fluorescence sensor array based on perylene probe monomer-excimer emission transition for the highly efficient differential sensing of metal ions and drinking waters, *Sens. Actuat. B Chem.* 319 (2020) 128212.
[13] A. Lealem Berhanu, Gaurav, I. Mohiuddin, A.K. Malik, J.S. Aulakh, V. Kumar, K. H. Kim, A review of the applications of Schiff bases as optical chemical sensors, *Trac. Trends Anal. Chem.* 116 (2019) 74–91.
[14] H. Kim, B.A. Rao, J. Jeong, S. Angupillai, J.S. Choi, J.O. Nam, C.S. Lee, Y.A. Son, A rhodamine scaffold immobilized onto mesoporous silica as a fluorescent probe for the detection of Fe(III) and applications in bio-imaging and microfluidic chips, *Sens. Actuat. B Chem.* 224 (2016) 404–412.
[15] W.P. Lustig, S. Mukherjee, N.D. Rudd, A.V. Desai, J. Li, S.K. Ghosh, Metal–organic frameworks: Functional luminescent and photonic materials for sensing applications, *Chem. Soc. Rev.* 46 (11) (2017) 3242–3285.
[16] Y.M. Guo, L.F. Zhang, S.S. Zhang, Y. Yang, X.H. Chen, M.C. Zhang, Fluorescent carbon nanoparticles for the fluorescent detection of metal ions, *Biosens. Bioelectron.* 63 (2015) 61–71.
[17] S.Y. Ding, M. Dong, Y.W. Wang, Y.T. Chen, H.Z. Wang, C.Y. Su, W. Wang, Thioether-based fluorescent covalent organic framework for selective detection and facile removal of mercury(II), *J. Am. Chem. Soc.* 138 (9) (2016) 3031–3037.
[18] C.W. Abney, J.C. Gilhula, K. Lu, W. Lin, Metal–organic framework templated inorganic sorbents for rapid and efficient extraction of heavy metals, *Adv. Mater.* 26 (47) (2014) 7993–7997.
[19] H.M. Wu, Y. Xiao, Y. Guo, S.J. Miao, Q.Q. Chen, Z. Chen, Functionalization of SBA-15 mesoporous materials with 2-acetylthiophene for adsorption of Cr(III) ions, *Micropor. Mesopor. Mater.* 292 (2020) 109754.
[20] B. Aguila, Q. Sun, J.A. Perman, L.D. Earl, C.W. Abney, R. Elzein, R. Schlaf, S.Q. Ma, Efficient mercury capture using functionalized porous organic polymer, *Adv. Mater.* 29 (31) (2017) 1700665.
[21] M. Zhao, S. Wang, H.S. Wang, P.R. Qin, D.J. Yang, Y.Y. Sun, F.L. Kong, Application of sodium titanate nanofibers as constructed wetland fillers for efficient removal of heavy metal ions from wastewater, *Environ. Pollut.* 248 (2019) 938–946.
[22] N.D. Rudd, H. Wang, E.M.A. Fuentes-Fernandez, S.J. Teat, F. Chen, G. Hall, Y.J. Chabal, J. Li, Highly efficient luminescent metal–organic framework for the simultaneous detection and removal of heavy metals from water, *ACS Appl. Mater. Interfaces* 8 (44) (2016) 30294–30303.
[23] Z.J. Li, H.D. Xue, Y.X. Ma, Q. Zhang, Y.C. Li, M. Xie, H.L. Qi, X.D. Zheng, Dual-functionalized fluorescent cationic organic network: Highly efficient detection and removal of dichromate from water, *ACS Appl. Mater. Interfaces* 11 (49) (2019) 46197–46204.
[24] X.L. Li, H. Lin, Q.L. Li, J.Y. Xue, Y. Xu, L. Zhuang, Recyclable magnetic fluorescent Fe_3O_4@SiO_2 core–shell nanoparticles decorated with carbon dots for fluoride ion removal, *ACS Appl. Nano Mater.* 4 (3) (2021) 3062–3074.
[25] W. Al Zoubi, M.P. Kamil, S. Fatimah, N. Nashrah, Y.G. Ko, Recent advances in hybrid organic–inorganic materials with spatial architecture for state-of-the-art applications, *Prog. Mater. Sci.* 112 (2020) 100663.
[26] D. Zhao, J. Feng, Q. Huo, N. Melosh, G.H. Fredrickson, B.F. Chmelka, G.D. Stucky, Triblock copolymer syntheses of mesoporous silica with periodic 50 to 300 angstrom pores, *Science* 279 (5350) (1998) 548–552.
[27] M. Gao, J. Zeng, K. Liang, D.Y. Zhao, B. Kong, Mesoporous silica materials: Interfacial assembly of mesoporous silica-based optical heterostructures for sensing applications, *Adv. Funct. Mater.* 30 (9) (2020) 2070057.
[28] N. Lashgari, A. Badiei, G. Mohammadi Ziarani, A novel functionalized nanoporous SBA-15 as a selective fluorescent sensor for the detection of multianalytes (Fe^{3+} and $Cr_2O_7^{2-}$) in water, *J. Phys. Chem. Solids* 103 (2017) 238–248.
[29] L.Y. Zhao, J.Y. Li, D. Sui, Y. Wang, Highly selective fluorescence chemosensors based on functionalized SBA-15 for detection of Ag^+ in aqueous media, *Sens. Actuat. B Chem.* 242 (2017) 1043–1049.
[30] E. Da'na, A. Sayari, Adsorption of copper on amine-functionalized SBA-15 prepared by co-condensation: Equilibrium properties, *Chem. Eng. J.* 166 (1) (2011) 445–453.
[31] M.R. Awual, M. Ismael, T. Yaita, S.A. El-Safty, H. Shiwaku, Y. Okamoto, S. Suzuki, Trace copper(II) ions detection and removal from water using novel ligand modified composite adsorbent, *Chem. Eng. J.* 222 (2013) 67–76.
[32] S. Parambadath, A. Mathew, M.J. Barnabas, S.Y. Kim, C.S. Ha, Concentration-dependant selective removal of Cr(III), Pb(II) and Zn(II) from aqueous mixtures using 5-methyl-2-thiophenecarboxaldehyde Schiff base-immobilised SBA-15, *J. Sol-Gel Sci. Technol.* 79 (3) (2016) 426–439.

[33] J. Wang, X.M. Zhang, H.B. Liu, D. Zhang, H.T. Nong, P.Y. Wu, P.X. Chen, D. Li, Aggregation induced emission active fluorescent sensor for the sensitive detection of Hg^{2+} based on organic–inorganic hybrid mesoporous material, *Spectrochim. Acta A* 227 (2020) 117585.
[34] H.B. Liu, Y.H. Liang, J. Liang, J. Wang, Q.Y. Li, Y.Y. Liu, Q.L. Li, Y.Q. Zhu, F.P. Dong, Pyrene derivative-functionalized mesoporous silica-Cu^{2+} hybrid ensemble for fluorescence "turn-on" detection of H_2S and logic gate application in aqueous media, *Anal. Bioanal. Chem.* 412 (4) (2020) 905–913.
[35] D.L. Li, K.G. Chai, X.D. Yao, L.Q. Zhou, K.Y. Wu, Z.H. Huang, J.T. Yan, X.Z. Qin, W. Wei, H.B. Ji, *β*-Cyclodextrin functionalized SBA-15 *via* amide linkage as a super adsorbent for rapid removal of methyl blue, *J. Colloid Interface Sci.* 583 (2021) 100–112.
[36] H.Z. Cui, Y.L. Li, S. Liu, J.F. Zhang, Q. Zhou, R. Zhong, M.L. Yang, X.F. Hou, Novel Pb(II) ion-imprinted materials based on bis-pyrazolyl functionalized mesoporous silica for the selective removal of Pb(II) in water samples, *Micropor. Mesopor. Mater.* 241 (2017) 165–177.
[37] J. Huang, H.B. Liu, J. Wang, Functionalized mesoporous silica as a fluorescence sensor for selective detection of Hg^{2+} in aqueous medium, *Spectrochim. Acta A* 246 (2021) 118974.
[38] M. Li, X.J. Jiang, H.H. Wu, H.L. Lu, H.Y. Li, H. Xu, S.Q. Zang, T.C.W. Mak, A dual functional probe for "turn-on" fluorescence response of Pb^{2+} and colorimetric detection of Cu^{2+} based on a rhodamine derivative in aqueous media, *Dalton Trans.* 44 (39) (2015) 17326–17334.
[39] Z.L. Gong, F. Ge, B.X. Zhao, Novel pyrazoline-based selective fluorescent sensor for Zn^{2+} in aqueous media, *Sens. Actuat. B Chem.* 159 (1) (2011) 148–153.
[40] T. Anand, S.K. Ashok Kumar, S.K. Sahoo, A new Al^{3+} selective fluorescent turn-on sensor based on hydrazide-naphthalic anhydride conjugate and its application in live cells imaging, *Spectrochim. Acta A* 204 (2018) 105–112.